Fluid Dynamics Research 6 (1990) 261–275
North-Holland

Experimental study of a three-dimensional large-scale structure in a reciprocating oscillatory flow

Mikio Hino

Department of Civil Engineering, Tokyo Institute of Technology, 2-12-1 O-okayama, Meguro-ku, Tokyo 152, Japan

Yu Fukunishi

Department of Mechanical Engineering II, Tohoku University, Aramaki-Aoba, Aoba-ku, Sendai 980, Japan

and

Yan Meng

Department of Civil Engineering, Tokyo Institute of Technology, 2-12-1 O-okayama, Meguro-ku, Tokyo 152, Japan

Received 17 October 1989

Abstract. An experimental investigation has been conducted on the large-scale structure of the reciprocating oscillatory turbulent flow in a rectangular duct. Using hot-wire anemometers and conditional sampling technique, we found that the Reynolds stress generated explosively in the decelerating phase, a characteristic feature of the flow, is caused by the three-dimensional large-scale structure. These structures are revealed to be a pair of counter-rotating fluid motions which change their form gradually as the phase-averaged velocity distribution changes. Phase differences of the turbulence intensity distribution in an oscillatory flow are found to take place in accordance with the generation–growth–decay process of the large-scale structure.

1. Introduction

Oscillatory flows are related to a variety of phenomena in science, engineering, and medicine, such as river flows in tidal estuaries, surging motion of water columns in a penstock, wave motions on the seabed, and blood flows in animals and human bodies.

The characteristics of such a flow are quite different from wall turbulence, which is steady in the mean. The generation–growth–decay process of turbulence is repeated by supplying artificially and periodically mechanical energy into the flow. Hino et al. (1983) provided detailed data on the statistical quantities of various phases and pointed out that turbulence in the accelerating phase was suppressed and could not develop, but that with the beginning of flow deceleration, turbulence and Reynolds stress grew violently and propagated towards the central part of the duct. However, the mechanism of the abrupt generation of turbulence and Reynolds stress has not been made fully clear.

In recent years, coherent motion in the fully developed turbulent boundary layer along a flat plate has been investigated extensively. The coherent motions were first observed in the wall region of the turbulent boundary layer by Kline et al. (1967), who found that low-velocity lumps of fluid move away from the wall. Later Corino and Brodkey (1969) further identified

0169-5983/90/$4.75

that high-speed lumps move toward the bottom. These motions were called "ejection" and "sweep", respectively. Quantitative analyses of the large-scale structure in turbulent flows were investigated by Kovasznay, Kibens and Blackwelder (1970), and in 1972 Blackwelder and Kovasznay analyzed a large-scale structure with the introduction of conditional sampling and time–space correlation. The results showed that averaged velocity inside a large-scale structure is lower than that of the surrounding flow and that the high Reynolds stress which plays a significant role in turbulence-energy production is intermittently generated by large-scale structures. The three-dimensional ensemble-averaged feature of a coherent structure was first studied by Fukunishi and Sato (1987a, 1987b) with conditional sampling technique; they showed that the coherent structures are pairs of counter-rotating fluid motions which they named the "banana-vortex-pair". For a large-scale structure in an unsteady flow, in contrast only a few investigations have been undertaken. Hino et al. (1983) showed spatial turbulence structures in an oscillatory flow using the time–space correlation method. However, the three-dimensional configuration of these structures and its relation with statistical quantities is not yet clear.

The purpose of our experiment is to investigate the three-dimensional configuration of a large-scale structure existing in a decelerating phase and throw new light on the mechanism of the abrupt generation of turbulence and Reynolds stress.

2. Experimental apparatus

2.1. Wind tunnel

The experiment was performed in a 14 m long reciprocating wind tunnel with a rectangular cross section of 26 cm × 10 cm (fig. 1). The rotary motion of an arm driven by a motor is converted by mechanical projection to a sinusoidal reciprocating motion, which derives a piston in the settling chamber (inner diameter 48 cm) of the wind tunnel. The air flow is regulated by honeycombs and screens in the settling chamber and driven, through a bellmouth of a 7 : 1 contraction ratio, into the wind tunnel. At the other end, the wind tunnel is opened to the air through a bellmouth and screen. The period of oscillatory motion is variable within a range of 2.5 to 53 s, and the stroke of the piston could be selected within the range of 15 to 30 cm. For details of the wind tunnel, the readers are referred to papers by Hino et al. (1983) and Meng et al. (1989).

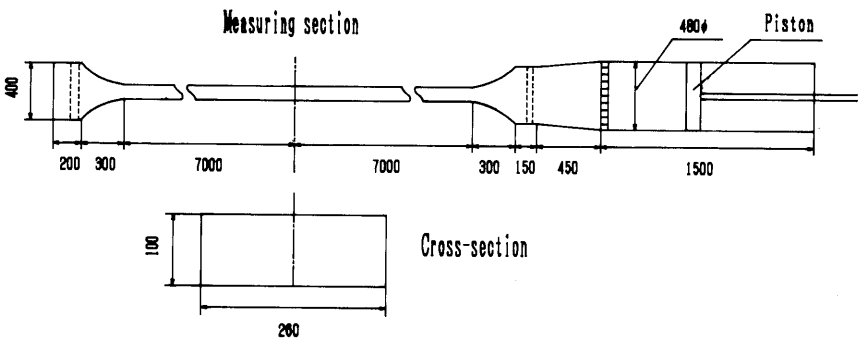

Fig. 1. Experiment apparatus: reciprocating oscillatory flow wind tunnel.

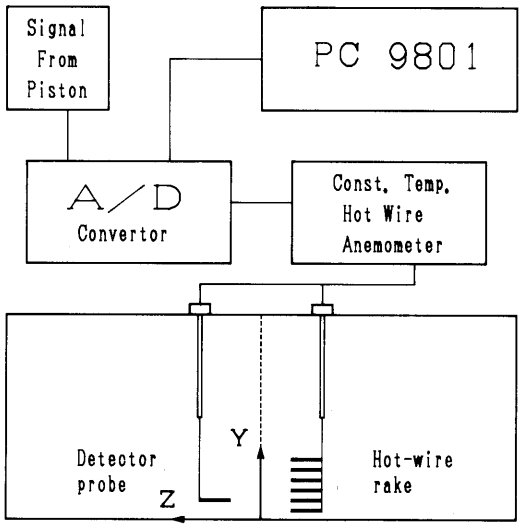

Fig. 2. A block diagram of the measurement system.

2.2. Experimental procedure

In this study, constant-temperature anemometers are the primary tool for data acquisition. One X-type probe was used for detecting the high Reynolds stress, and two different hot-wire-rake configurations were employed to simultaneously measure u–v and u–w components at a number of locations. The y-rake is utilized to measure simultaneously the normal distribution of u–v velocity components. The rake consists of 6 X-type probes, and the sensor distances from the bottom of the wall are 5, 10, 15, 20, 25 and 30 mm. The z-rake, used to measure the spanwise distribution of u–w velocity components, has 6 X-type probes with a center-to-center distance of 5 mm. The sensors were made of tungsten wire 5 μm in diameter and were used at a 0.5 overheat throughout this investigation. A frequency response typically greater than 10 kHz was achieved by using the familiar square test. Hot-wire calibration is accomplished by a laser-Doppler velocimeter equipped with a frequency shifter for distinguishing the flow direction. The velocity U is the function of the signals E out of the hot-wire anemometer and is represented by the relation

$$U = aE^3 + bE^2 + cE + d, \tag{1}$$

where a, b, c, d are constant and are determined by the least-squares method. The hot-wire outputs were digitized into 12-bit digits at the sampling frequency of 1 kHz per channel, and these data were recorded and analyzed by a personal computer (NEC-9801) with 4 Mbyte memory. The block diagram of the measurement system and the coordinate system used for the various measurements are given in fig. 2.

The experimental conditions are set up within the turbulence range. The amplitude of the cross-sectional mean velocity (U) and the period of oscillation (T) are 2.57 m/s and 3.15 s respectively. The Reynolds number based on the Stocks-layer thickness $\delta = (2\nu/\omega)^{1/2}$ (3.87 mm) (ν = kinematic viscosity, ω = angular frequency of oscillation), R_δ ($= U\delta/\nu$), is 710, and the Reynolds number is defined by depth of wind tunnel d, R_e ($= Ud/\nu$) being 1.84×10^4. The Stocks parameter $\lambda = d/2\delta$ is 12.9. Coordinates are normalized by the depth of wind tunnel d.

3. Phase-averaged statistics

3.1. Definitions

The phase-averaged velocity is defined in terms of the vertical distance y and of the phase ωt as

$$\bar{u}_i(y, \omega t) = \frac{1}{N} \sum_{k=0}^{N-1} u_i(x, y, z, \omega(t + kT)). \tag{2}$$

Instantaneous velocity fluctuations u_i' are defined as the difference of instantaneous velocities from the phase-averaged $\bar{u}_i$:

$$u_i'(x, y, z, \omega(t + kT)) = u_i(x, y, z, \omega t') - \bar{u}_i(x, y, z, \omega t'), \tag{3}$$

where $i = 1$, 2, and 3, $u_1 = u$, $u_2 = v$ and $u_3 = w$, and time t' is related to period T and phase ωt $(= 2\pi t/T)$:

$$\omega t' = \omega(t + kT) \quad (k = 0, 1, 2, \ldots). \tag{4}$$

The phase-averaged turbulent intensities and the phase-averaged Reynolds shear stress are defined in terms of position (x, y, z) and phase ωt as

$$\left(\overline{u'^2}\right)^{1/2}(x, y, z, \omega t') = \left(\frac{1}{N} \sum_{k=0}^{N-1} u'^2(x, y, z, \omega(t + kT)) \right)^{1/2}, \tag{5}$$

$$\left(\overline{v'^2}\right)^{1/2}(x, y, z, \omega t') = \left(\frac{1}{N} \sum_{k=0}^{N-1} v'^2(x, y, z, \omega(t + kT)) \right)^{1/2}, \tag{6}$$

$$\overline{-u'v'}(x, y, z, \omega t') = -\frac{1}{4N} \sum_{k=0}^{4N-1} u'(x, y, z, \omega(t + kT)) v'(x, y, z, \omega(t + kT)), \tag{7}$$

where N means the number of consecutively sampled waves and is 128. All of the phase-averaged statistics are normalized by the amplitude of the cross-sectional mean velocity.

3.2. Phase-averaged velocity distribution

The profiles of the phase-averaged velocity for various phases are shown in fig. 3. At the beginning of the flow acceleration, the velocity near the wall is larger than that near the center.

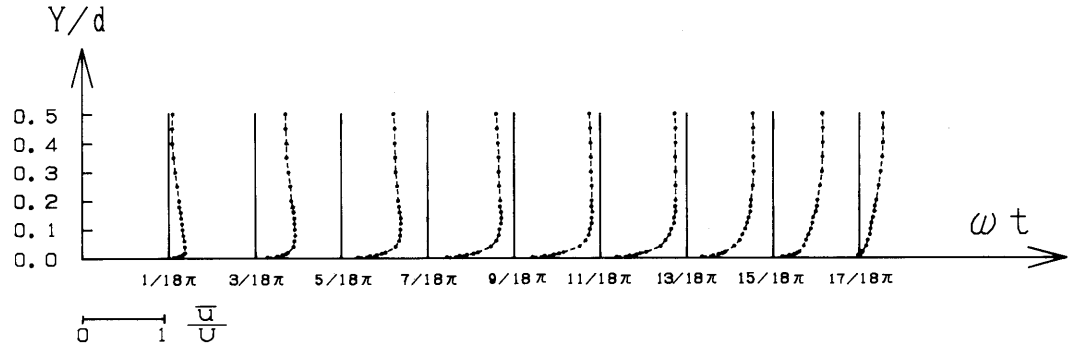

Fig. 3. Vertical profiles of the phase-averaged velocity distribution at various phases.

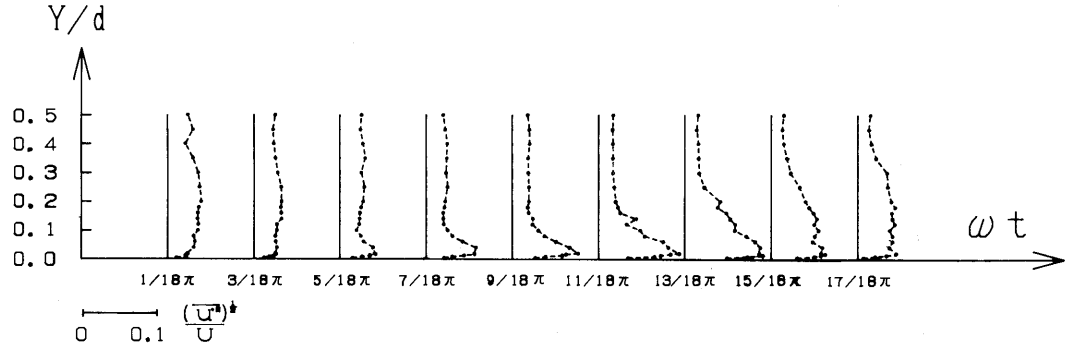

Fig. 4. Vertical profiles of the u'_{rms} turbulence velocity fluctuations.

In the phase of $\omega t = \frac{9}{18}\pi$, the phase-averaged velocity profile is similar to that of the ordinary turbulent boundary layer. With phase advance, the velocity profile changes gradually, and the phase differences of the vertical distribution of velocity plays a significant role in the deformation of the large-scale structure, as shown subsequently.

3.3. Turbulence intensities

The profiles of the vertical distributions of turbulence intensities $(\overline{u'^2})^{1/2}/U$ and $(\overline{v'^2})^{1/2}/U$ at various phases are given in figs. 4 and 5.

Vertical profiles of $(\overline{u'^2})^{1/2}/U$ in the early phase of acceleration are nearly uniform, but with the advance of phase, the turbulence intensity decreases from the wall towards the channel center. In the decelerating phase, $(\overline{u'^2})^{1/2}/U$ grows explosively from the bottom and shows a maximum value at the phase $\omega t = \frac{13}{18}\pi$; then it becomes smaller again as the cross-sectional mean velocity decreases.

The vertical profiles of $(\overline{v'^2})^{1/2}/U$ near the bottom in the early phase of acceleration are quite small, in spite of the value of the turbulence intensity at a given distance from the bottom. With phase advance the value of the $(\overline{v'^2})^{1/2}/U$ near the bottom becomes larger gradually. In the decelerating phase, $(\overline{v'^2})^{1/2}/U$ grows from the bottom and shows a maximum value in the phase of $\omega t = \frac{13}{18}\pi$; then they become smaller again as the cross-sectional mean velocity decreases.

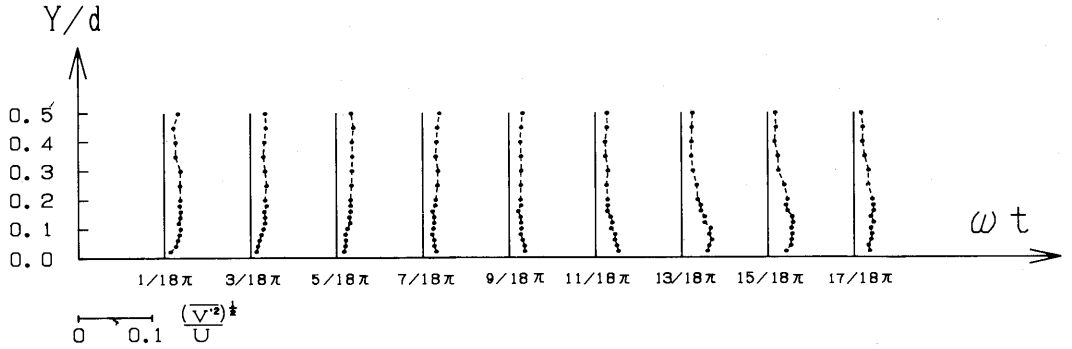

Fig. 5. Vertical profiles of the v'_{rms} turbulence velocity fluctuations.

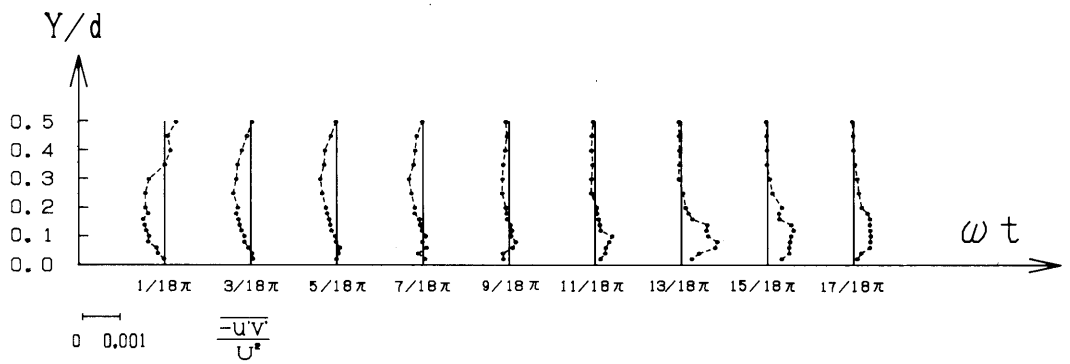

Fig. 6. Vertical profiles of the Reynolds stress $-\overline{u'v'}/U^2$ at various phases.

3.4. Reynolds stress

The phase-averaged Reynolds stress divided by ρU^2, $-\overline{u'v'}/U^2$, at various depths is plotted in fig. 6. The Reynolds stress near the bottom is almost negligible at the initial stage of acceleration ($\omega t = (\frac{2}{18} - \frac{7}{18})\pi$), but at a distant region from the bottom, relatively large negative values appear. With phase advance, the Reynolds stress at the region for from the bottom decreases, while the values of the Reynolds stress near the bottom increase gradually. With the beginning of flow deceleration, the Reynolds stress grows explosively in the region at a slight distance from the bottom and reaches a maximum value at the phase $\omega t = \frac{13}{18}\pi$. Then it decreases over the whole cross section with the flow deceleration, and propagates towards the central part of the wind tunnel. The results show that the Reynolds stress generated in the decelerating phase plays a significant role in turbulence-energy production.

4. A large-scale structure in oscillatory flow

4.1. Instantaneous flow fields

To investigate the cause of the explosive generation of the Reynolds stress near the bottom from the beginning of the flow deceleration phase, multi-point simultaneous measurements at six y locations were made using the y-rake described previously. Fig. 7 shows an example of simultaneous traces of velocity fluctuations u' and v' and the instantaneous Reynolds stress $-u'v'$. The peaks of Reynolds stress appear in the decelerating phase, and the simultaneous velocity fluctuations corresponding to those peaks have a very strong correlation. Although turbulence with a perceivable intensity is observed even in the accelerating phase, the instantaneous Reynolds stress ($-u'v'$) which carries the momentum transport is negligible. These results imply that in the accelerating phase, no large-scale structure which contributes to instantaneous high Reynolds stress exists and no instantaneous large turbulence energy production occurs. This is the reason why the turbulence intensity decreases gradually with the advance of the accelerating phase. So in this study we concentrated our attention on the instantaneous high Reynolds stress generated in the decelerating phase.

4.2. Conditional sampling

In order to obtain information on the large-scale structure which produces the high Reynolds stress in the decelerating phase, the conditional sampling technique was used. A

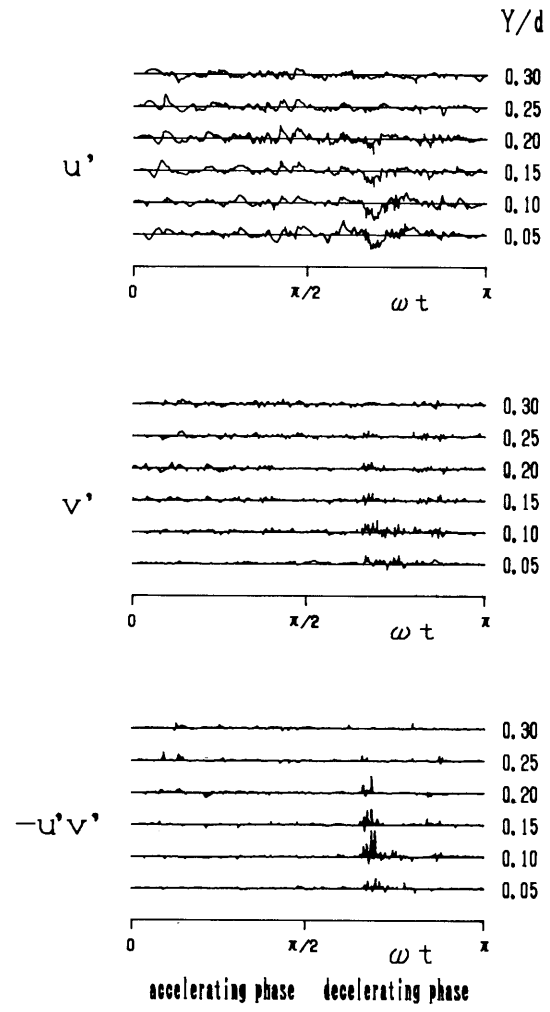

Fig. 7. Simultaneous traces of velocity fluctuations u', v' and the instantaneous Reynolds stress $-u'v'$.

detector probe (X-type hot-wire) was set at $Y/d = 0.1$ depth where large Reynolds stress according to the four-quadrant identification criterion was extracted. The Reynolds stress from the detector probe was smoothed by computing the moving averages. The preliminary experiment showed that the ensemble-averaged results were not sensitive to high cut-off frequencies, so the cut-off frequency was set at 25 Hz. Another parameter is the threshold of Reynolds stress. A little attention should be paid to determining the level of the threshold, because if the threshold is too high, only extremely unusual structures are detected, but if it is too low, the structures are smeared out in the process of averaging. In this study, we chose three times the value of phase-averaged Reynolds stress at depth $Y/d = 0.1$ as the threshold at that phase. When the value of the Reynolds stress peak was larger than the threshold, data temporarily recorded in the memory were saved from 50 ms ahead to 50 ms after the detection, and 100 samples were used to obtain one ensemble average. The schematic diagram of the conditional sampling process is shown in fig. 8. From the preliminary experiment, we noticed that in the

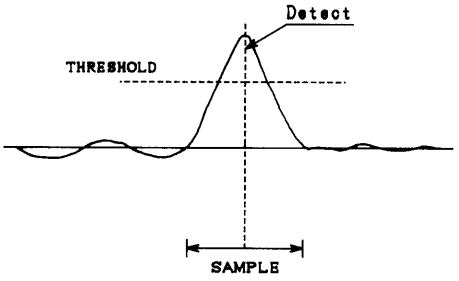

Fig. 8. A schematic diagram of the conditional sampling procedure.

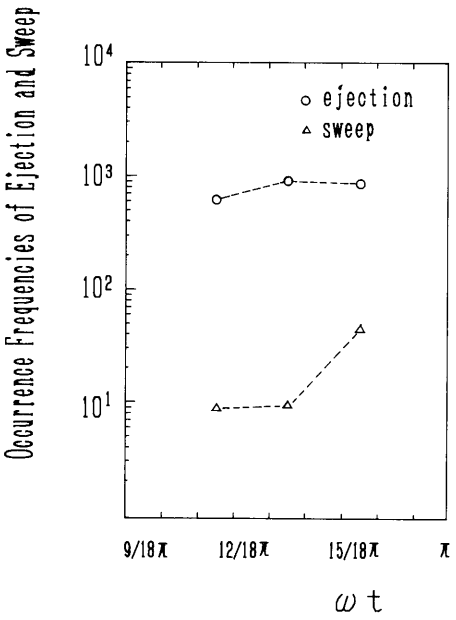

Fig. 9. Frequencies of appearance of ejection-type and sweep-type motions in the semi-logarithmic plot. (counts per 2000 events).

deceleration phase, most of the high Reynolds stress is produced by ejection-type motions. Fig. 9 shows frequencies of appearance of the ejection type and the sweep type motions in the semi-logarithmic plot. In this study, we concentrate on the ejection motions.

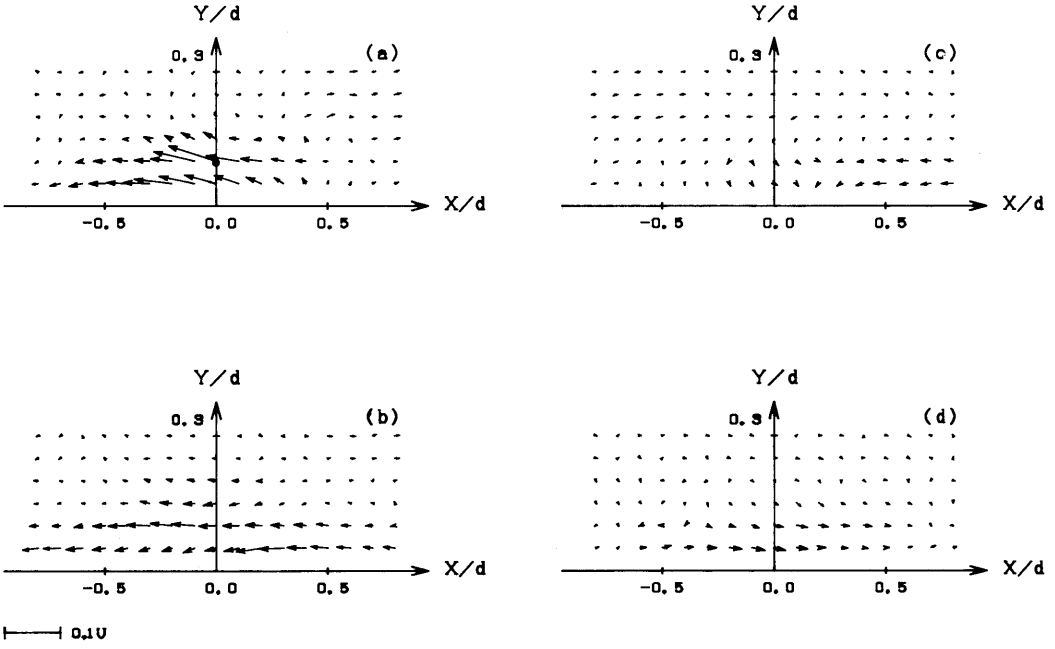

Fig. 10. Ensemble-averaged u, v vectors in various (X, Y)-planes at the phase $\omega t = (\frac{9}{18} - \frac{10}{18})\pi$. (a) $Z/d = 0.00$, (b) $Z/d = -0.05$, (c) $Z/d = -0.10$, (d) $Z/d = -0.15$.

4.3. Spatial distribution of the velocity fluctuation

In order to determine the fluid motions surrounding the detector probe, a y-rake was moved to various spanwise locations to take in u–v velocity components data. Considering the turbulence fluctuations as a stationary and ergodic random process during a short interval in a given phase, time traces can be changed into spatial data by applying Taylor's hypothesis of frozen eddies. Figs. 10a–10d show the ensemble-averaged u, v velocity fluctuation vectors in various (X, Y)-planes at phase $\omega t = (\frac{9}{18} - \frac{10}{18})\pi$. The ordinate axis corresponds to the time when large Reynolds stress is detected and the abscissa is X. The solid circle in fig. 10a shows the position of the detector probe. The arrows in the vicinity of the detector probe are directed upward toward the left, indicating that the low-speed fluid moves away from the bottom, but the arrows shown in the (X, Y)-plane at $Z/d = -0.05$ become smaller, and thus those plotted in the (X, Y)-plane at $Z/d = -0.10$ have negligible values. Fig. 10d shows the ensemble-averaged u, v vectors at the $Z/d = -0.15$ section, in which the arrows pointing downwards to the right can be found. In other words, the high-speed flow moves toward the bottom in that section, which is 15 mm away from the detector probe.

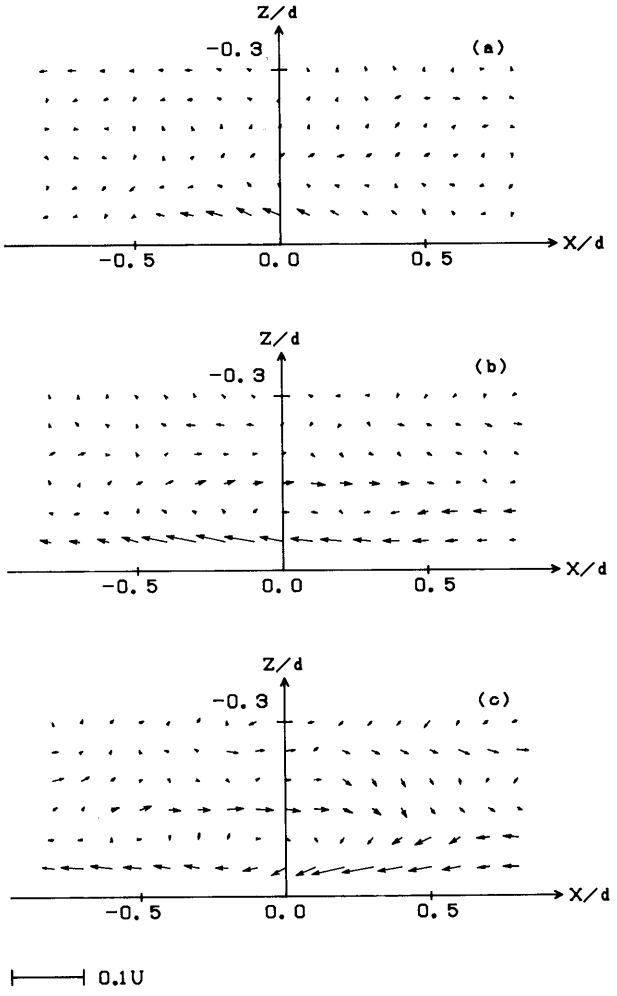

Fig. 11. Ensemble-averaged u, w vectors in various (X, Z)-planes at the phase $\omega t = (\frac{9}{18} - \frac{10}{18})\pi$. (a) $Y/d = 0.15$, (b) $Y/d = 0.10$, (c) $Y/d = 0.05$.

Next, u and w components are measured by the z-rake in various (X, Z)-planes with the same detection method. Figs. 11a–11c show the ensemble-averaged u, w velocity fluctuation vectors in various (X, Z)-planes at the same phase. A rotating flow can be found in figs. 11a, 11b, but in the (X, Z)-plane shown in fig. 11c, the rotating flow becomes weak. Considering that the results are symmetrical about the vertical plane of $Z/d = 0$ where the detector probe is set, only the half having negative z is shown. The reason is that although an individual structure may not be symmetrical with respect to the detection plane, turbulent events with a large-scale structure passing through the point may occur with uniform probability.

4.4. Spatial distribution of the vorticity

In order to describe the three-dimensional configuration of the large-scale structure, the vorticities have been computed from ensemble-averaged velocity components. The contours of ω_y vorticity in various (X, Z)-planes at the phase $(\frac{9}{18}-\frac{10}{18})\pi$ are shown in figs. 12a–12d. Solid lines are contours of negative (clockwise rotation) vorticity, and broken lines are positive (counterclockwise rotation) ones. The ω_y contours have values ranging from -20 to -4 in increments of 4. Strong ω_y components exist in the planes near the bottom, and the centers of rotations in the planes closer to the bottom tend to be shifted upstream. Figs. 13a–13d illustrate contours of ω_x vorticity in various (Y, Z)-planes at various streamwise distances perpendicular to the mean flow. The contours in the upstream (Y, Z)-plane at $X/d = -0.2$ give large values, and the center of rotation closes to the bottom, which indicates the leg of the structure, exists in that region. From figs. 12 and 13 of longitudinal and vertical cross sections of vorticity, we can draw an image of a rotating vortex pair as shown in fig. 14. Such features of the structure detected at the phase $(\frac{9}{18}-\frac{10}{18})\pi$ are qualitatively in good agreement with the coherent motions in an ordinary turbulent boundary layer, which is called the banana-vortex-pair (Fukunishi and Sato, 1987).

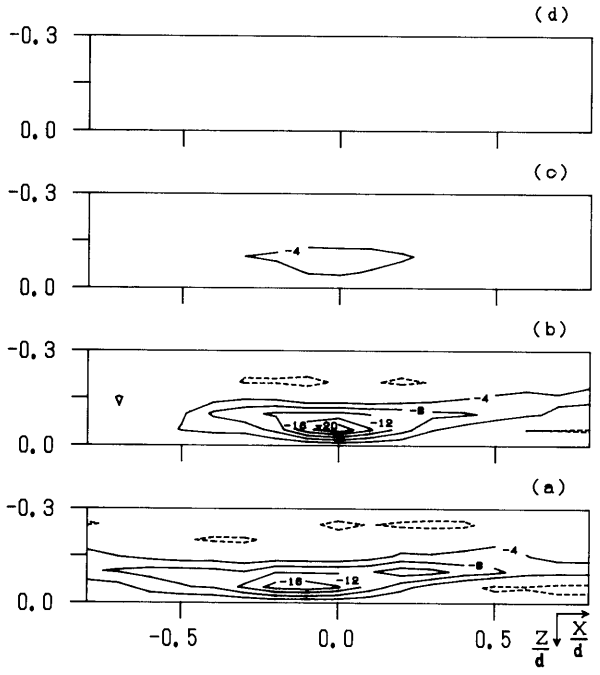

Fig. 12. Contours of vorticity component ω_y (s^{-1}) in various (X, Z)-planes at the phase $(\frac{9}{18}-\frac{10}{18})\pi$. (a) $Y/d = 0.05$, (b) $Y/d = 0.10$, (c) $Y/d = 0.15$, (d) $Y/d = 0.20$.

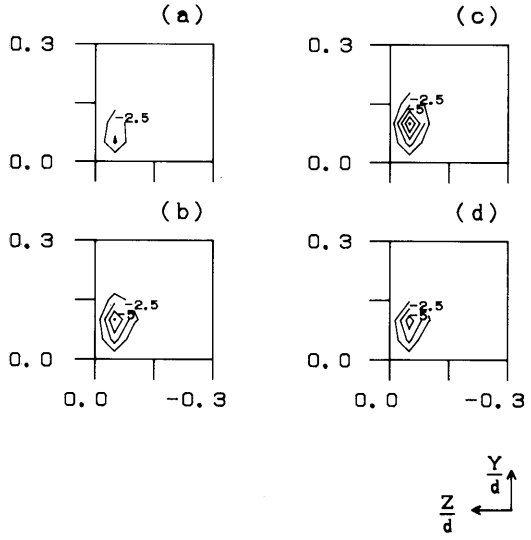

Fig. 13. Contours of vorticity component ω_x (s^{-1}) in various (Y, Z)-planes at the phase $(\frac{9}{18}-\frac{10}{18})\pi$. (a) $X/d=-0.2$, (b) $X/d=-0.1$, (c) $X/d=0.0$, (d) $X/d=0.1$.

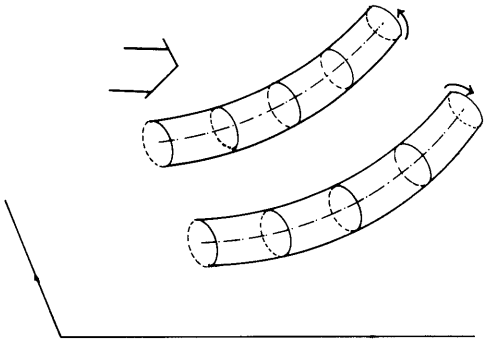

Fig. 14. An image of a rotating vortex pair.

5. Phase variation of a large-scale structure

A characteristic feature of oscillatory flow is that a pressure gradient exists, a favorable one in the accelerating phase and an adverse one in the decelerating phase. The distribution of the phase-averaged velocity changes with the advance of the phase. The effect of pressure gradient on the large-scale structure is a very interesting problem, and only a few investigations have been conducted until recently. In this experiment, we investigated a large-scale structure in various phases and attempted to find the relation between the structure and the turbulence statistics.

5.1. Phase variations of the distribution of the velocity fluctuation

The three-dimensional configuration of the large-scale structure at various phases was investigated with the same approach described in section 4. The results measured at two typical

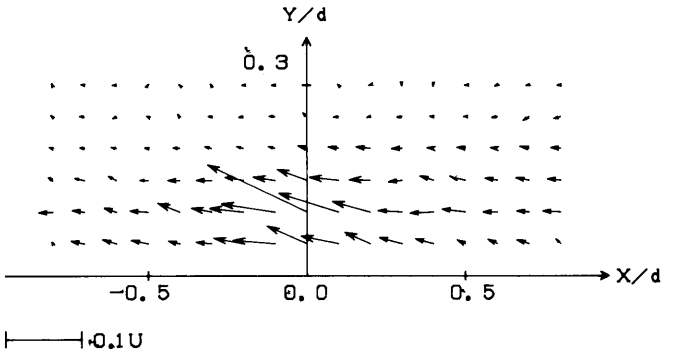

Fig. 15. Ensemble-averaged u, v velocity vectors in the (X, Y)-plane for $Z/d=0.0$ at phase $(\frac{12}{18}-\frac{13}{18})\pi$.

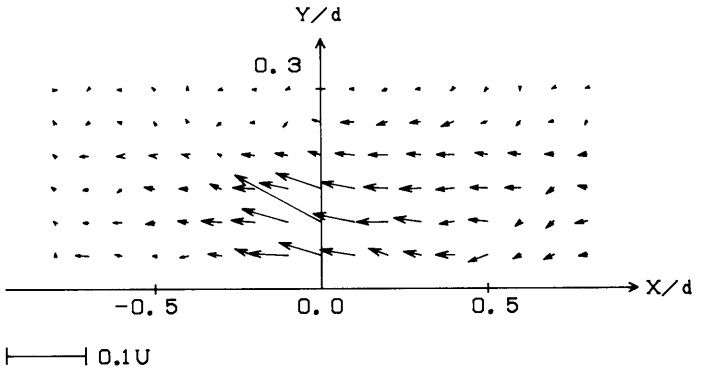

Fig. 16. Ensemble-averaged u, v velocity vectors in the (X, Y)-plane for $Z/d = 0.0$ at phase $(\frac{14}{18}-\frac{15}{18})\pi$.

phases will be discussed here. Figs. 15 and 16 give the ensemble-averaged values of u, v velocity fluctuation vectors in the (X, Y)-plane for $Z/d = 0.0$ at the phase $\omega t = (\frac{12}{18}-\frac{13}{18})\pi$ and $\omega t = (\frac{14}{18}-\frac{15}{18})\pi$. Both of them show that the low-speed flow moving away from the bottom exists, and this feature does not change with the advance of phase. However, the strength of the ensemble-averaged fluctuations accompanying these structures changed with the advance of phase as can be seen in fig. 17 showing changes in absolute maximum of ensemble-averaged u, v at the instant of the detection for ejection motion. In the early phase $(\frac{9}{18}-\frac{10}{18})\pi$ these structures are weak, but in the middle phase $(\frac{12}{18}-\frac{13}{18})\pi$ they become stronger and in the final phase $(\frac{14}{18}-\frac{15}{18})\pi$ they weaken again.

In order to work out the relation between change in a large-scale structure and the phase differences of the turbulence intensity, a comparison of turbulence intensity with the large-scale structure was made. The vertical profiles of the velocity fluctuations u at the instant of the detection for the ejection motion are compared with the distributions of the turbulence intensity u'_{rms} for the whole periods of turbulent bursting motions including the ejection, sweep and interactions at corresponding phases (shown in fig. 18). We found that the changes in the

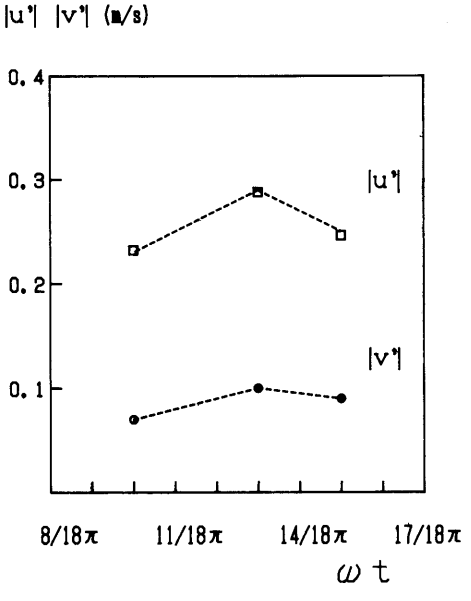

Fig. 17. Changes in the absolute maximum of velocity fluctuations u and v at the instant of the detection for the ejection motion.

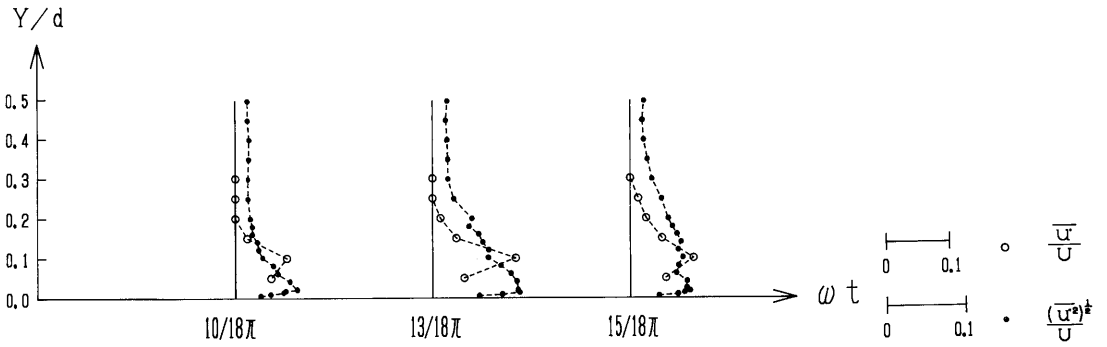

Fig. 18. Vertical profiles of the velocity fluctuations u at the instant of the detection for the ejection motions (○) compared with the profiles of the turbulence intensity u'_{rms} for the whole turbulent motion (●).

turbulent statistics are in good agreement with the variations in the structures. These results show that the phase differences of the turbulence statistics can be explained by the variations of the large-scale structure detected in the decelerating phases.

5.2. *Phase variations of the distribution of the vorticity*

Figs. 19a–19d show contours of the vorticity component ω_y in various (X, Z)-planes at the phase $(\frac{12}{18}-\frac{13}{18})\pi$. A strong vorticity area appears in the (X, Z)-plane at $Y/d = 0.15$, and the central lines of vorticity are less inclines compared with fig. 12. Figs. 20a–20d give the contours of the vorticity component ω_y in various (X, Z)-planes at the phase $(\frac{14}{18}-\frac{15}{18})\pi$. Strong vorticity can be found in the $(X, Z-$ -plane at greater distance from the bottom $(Y/d = 0.2)$. These results imply that these structures become "taller". In order to make a clear comparison, axes

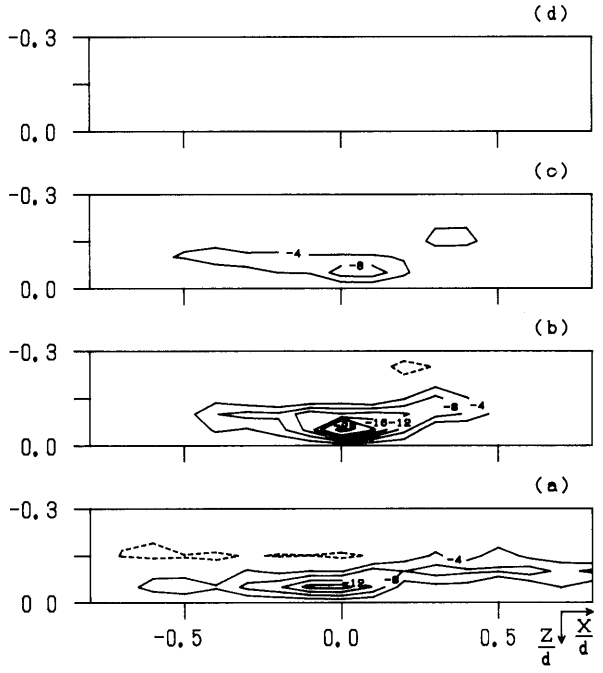

Fig. 19. Contours of vorticity component ωy (s^{-1}) in various (X, Z)-planes at the phase $(\frac{12}{18}-\frac{13}{18})\pi$. (a) $Y/d = 0.05$, (b) $Y/d = 0.10$, (c) $Y/d = 0.15$, (d) $Y/d = 0.20$.

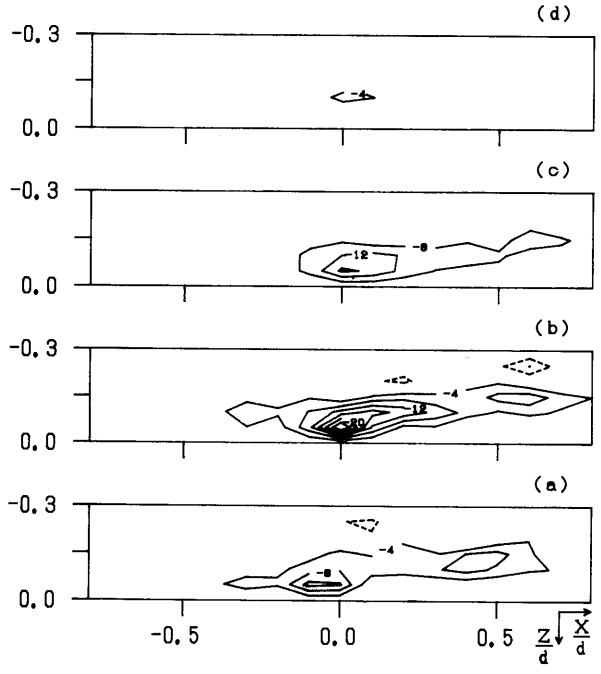

Fig. 20. Contours of vorticity component ω_y (s^{-1}) in various (X, Z)-planes at the phase $(\frac{14}{18}-\frac{15}{18})\pi$. (a) $Y/d = 0.05$, (b) $Y/d = 0.10$, (c) $Y/d = 0.15$, (d) $Y/d = 0.20$.

of vortical motion with vorticity ω_y at various phases have been computed and are shown in fig. 21. With the advance of phase, the average height of the structure becomes "taller" and the structure becomes less inclined.

It was noticed that the large-scale structures found in the decelerating phase change not only their strength but also their size, form, and inclination. The variations of these structures may be divided into three processes, shown in fig. 22. In the accelerating phase, no large-scale structure exists, but with the beginning of the decelerating phase, the large-scale structure which generates the high Reynolds stress is first detected, so we regard the initial phase of the deceleration flow as the generation process of the structure. With the advance of time from the initial phase, the vortical structure, which is stretched by the strong velocity gradient, gains in strength and achieves a maximum value at a phase $(\frac{12}{18}-\frac{13}{18})\pi$. This stage can be thought of as

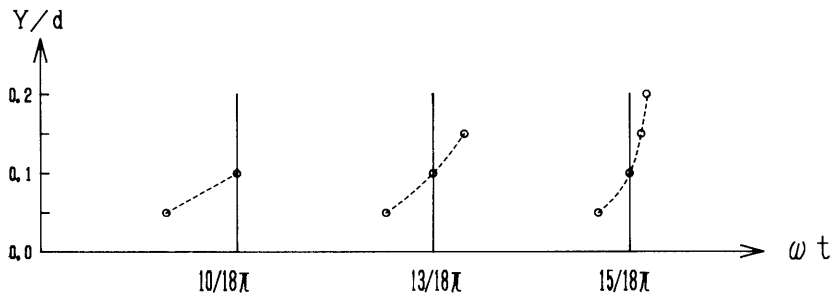

Fig. 21. Axes of vortical motion with vorticity ω_y at various phases.

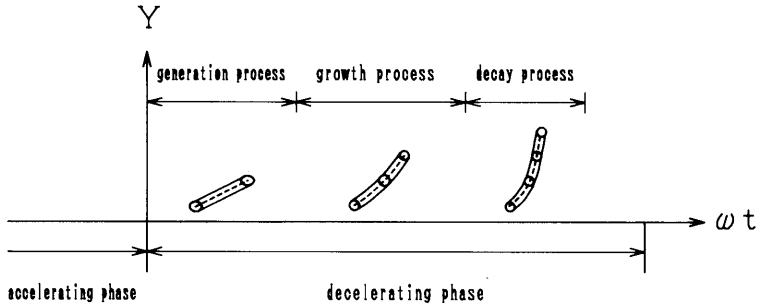

Fig. 22. A schematic picture of the generation–growth–decay process of a large-scale structure.

the growth process. In the final phase, the velocity gradient becomes weaker and the large-scale structure is weakened. This stage may be called the decay process.

6. Conclusions

From this study, the following conclusions were obtained.

(1) The Reynolds stress in a turbulent oscillatory flow with zero-mean velocity is generated intermittently in the deceleration phase, and most of the high Reynolds stress are produced by the ejection-type motions.

(2) The structures of the turbulence are pairs of counter-rotating fluid motion which change their form gradually as the phase-averaged velocity profile changes.

(3) In the early phase these structures are weak, but as the deceleration phase proceeds they become stronger and then weaker again. With the advance of phase, these structures change not only their strength but also their form. The average height of the structure gets taller, and the structure is less inclined.

(4) Phase differences of the turbulence intensity distribution in an oscillatory flow are found to take place in accordance with the generation–growth–decay process of a large-scale structure.

References

Blackwelder, R.F., and W.S.G. Kovasznay (1972) Large-scale motion of a turbulent boundary layer during relaminarization, *J. Fluid Mech. 63*, 61–83.

Corino, E.R. and R.S. Brodkey (1969) A visual investigation of the wall region in turbulent flow, *J. Fluid Mech. 37*, 1–30.

Fukunishi, Y. and H. Sato (1987a) Formation of intermittent region by coherent motions in the turbulent boundary layer, *Fluid Dyn. Res. 2*, 113–124 (translated from: Nagare, J. Japan Soc. Fluid Mechanics 2 (1983) 272–287, in Japanese).

Fukunishi, Y. and H. Sato (1987b) Study of developing process of coherent structures in the turbulent boundary layer, *AIAA 19th Fluid Dynamics*.

Kline, S.J., W.C. Reynolds, F.A. Schraub and P.W. Runstadler (1967) The structure of turbulent boundary layers, *J. Fluid Mech. 30*, 741–773.

Kovasznay, L.S.G., V. Kibens and R.F. Blackwelder (1970) Large-scale motion in the intermittent region of a turbulent boundary, *J. Fluid Mech. 41*, 283–325.

Hino, M., M. Kashiwayanagi, A. Nakayama and T. Hara (1983) Experiments on the turbulence statistics and the structure of a reciprocating oscillatory flow, *J. Fluid Mech. 131*, 363–400.

Meng, Y., M. Hino and Y. Fukunishi (1989) Experiment on the large-scale structure in a reciprocating oscillatory flow, *Proc. 4th Asian Congress of Fluid Mechanics*.